PNAS Nexus

PNAS Nexus, 2022, **2**, 1–12
https://doi.org/10.1093/pnasnexus/pgac298
Advance access publication date: 16 December 2022
Research Report

High-resolution cryo-EM structure of the junction region of the native cardiac thin filament in relaxed state

Cristina M. Risi[a], Betty Belknap[a], Howard D. White[a], Kelly Dryden[b], Jose R. Pinto[c], P. Bryant Chase[d] and Vitold E. Galkin[a,*]

[a]Department of Physiological Sciences, Eastern Virginia Medical School, Norfolk, VA 23507, USA
[b]Department of Molecular Physiology and Biological Physics, University of Virginia, Charlottesville, VA 22904, USA
[c]Department of Biomedical Sciences, Florida State University College of Medicine, Tallahassee, FL 32304, USA
[d]Department of Biological Science, Florida State University, Tallahassee, FL 32306, USA
*To whom correspondence should be addressed: Email: galkinve@evms.edu
Edited By: Josh Wand

Abstract

Cardiac contraction depends on molecular interactions among sarcomeric proteins coordinated by the rising and falling intracellular Ca^{2+} levels. Cardiac thin filament (cTF) consists of two strands composed of actin, tropomyosin (Tm), and equally spaced troponin (Tn) complexes forming regulatory units. Tn binds Ca^{2+} to move Tm strand away from myosin-binding sites on actin to enable actomyosin cross-bridges required for force generation. The Tn complex has three subunits—Ca^{2+}-binding TnC, inhibitory TnI, and Tm-binding TnT. Tm strand is comprised of adjacent Tm molecules that overlap "head-to-tail" along the actin filament. The N-terminus of TnT (e.g., TnT1) binds to the Tm overlap region to form the cTF junction region—the region that connects adjacent regulatory units and confers to cTF internal cooperativity. Numerous studies have predicted interactions among actin, Tm, and TnT1 within the junction region, although a direct structural description of the cTF junction region awaited completion. Here, we report a 3.8 Å resolution cryo-EM structure of the native cTF junction region at *relaxing* (pCa 8) Ca^{2+} conditions. We provide novel insights into the "head-to-tail" interactions between adjacent Tm molecules and interactions between the Tm junction with F-actin. We demonstrate how TnT1 stabilizes the Tm overlap region via its interactions with the Tm C- and N-termini and actin. Our data show that TnT1 works as a joint that anchors the Tm overlap region to actin, which stabilizes the *relaxed* state of the cTF. Our structure provides insight into the molecular basis of cardiac diseases caused by missense mutations in TnT1.

Significance Statement:

Cardiac contraction depends on interactions between thin and thick filaments. Thin filament (TF) is comprised of actin, tropomyosin (Tm), and troponin (Tn) complex. The Tn complex, consisting of Ca^{2+}-binding TnC, inhibitory TnI, and Tm-binding TnT subunits, regulates thin and thick filaments interactions in a Ca^{2+}-dependent manner by moving Tm cable away from myosin binding sites on actin. TnT stabilizes the interaction between adjacent Tm molecules to form TF junction region. We report a 3.8 Å resolution cryo-EM structure of the native TF junction region that provides novel insights into normal diastolic function of the TF and elucidates the molecular basis of cardiac diseases caused by missense mutations in TnT.

Introduction

Cardiac contraction and subsequent relaxation is precisely regulated by cyclic fluctuations in Ca^{2+} levels that control force generation via actomyosin interactions between thin (actin-based) and thick (myosin-based) filaments (1–3). The backbone of the cardiac thin filament (cTF) is formed by filamentous actin (F-actin) that accommodates TF regulatory proteins—tropomyosin (Tm) that blocks actomyosin interactions at low Ca^{2+}, and the troponin (Tn) complex that governs the position of Tm on F-actin in a Ca^{2+}-dependent manner (3–6). Striated muscle Tm (α-Tm) is an α-helical protein that forms a parallel two-stranded coiled-coil dimeric molecule (7, 8). Tm molecules polymerize along the actin helix (9, 10) in a head-to-tail manner (11). Sequences of coiled-coil proteins, such as Tm, contain a seven-residue heptad repeat designated as *a*, *b*, *c*, *d*, *e*, *f*, and *g* with hydrophobic residues within the interface of the two α-helices located at positions *a* and *d* and charged residues at positions *e* and *g* that form interhelical salt bridges [reviewed in ref. (12)]. Each α-Tm molecule spans the length of seven actin subunits in the actin filament and has been assigned a seven-quasi-equivalent-period repeat (periods 1 to 7 or P1 to P7) (13) containing a pattern of amino acid residues predicted to be conserved actin-binding sites (14–16). Solution nuclear magnetic resonance (NMR) structure of the junction between two Tm model peptides showed that the C-terminal coiled-coil spreads apart to form a binding cleft for the 11 amino acids of the N-terminal coiled-coil, allowing Tm to form a continuous cable, with two such cables twisting around opposing sides of F-actin (17). Nevertheless, the existence of these interactions within the native TF has not yet been demonstrated.

Competing Interest:The authors declare no competing interest.
Received: October 12, 2022. **Accepted:** December 15, 2022

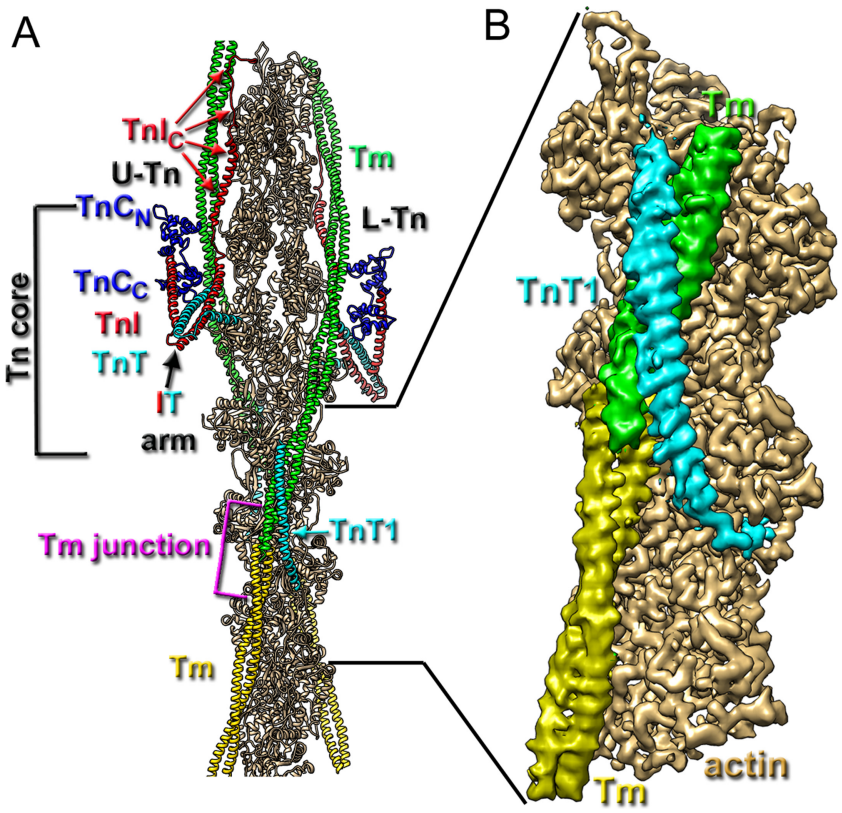

Fig. 1. The structural details of the cardiac TF and 3D reconstruction of its junction region at low Ca^{2+} (pCa 8). (A) The model of the cTF. The backbone of the cTF is comprised of actin (tan ribbons). Components of the Tn complex, which include TnC, TnI, and TnT are shown as blue, red, and cyan ribbons, respectively. Two consecutive Tm molecules are shown as green and gold ribbons. TnT is a part of both Tn core (black square bracket) and junction region (magenta square bracket). The two unequal Tn complexes are marked as upper (U-Tn) and lower (L-Tn). (B) The 3D reconstruction of the junction region is shown at 3.8 Å resolution using colored codes from (A). The barbed end of actin is at the bottom.

Regulation of actomyosin interactions by Ca^{2+}-dependent movement of the Tm cable on the surface of F-actin by the Tn complex is described by the steric blocking model, which holds that Tm blocks myosin binding sites on the surface of actin at *relaxing* conditions (low Ca^{2+}), whereas Tm moves away from the myosin binding sites at *activating* (elevated Ca^{2+}) conditions (4, 18). Therefore, the inhibited state of the cTF is called off state, while the activated state is referred to as on state. The multidomain Tn complex is comprised of three subunits—troponin I (TnI; the inhibitory subunit), troponin C (TnC; the Ca^{2+}-binding subunit), and troponin T (TnT; the Tm-binding subunit) [reviewed in refs. (19) and (20)]. Recent advances in cryo-EM enabled determination of the structures of reconstituted (5) and native (6) cardiac TFs in the Ca^{2+}-free and Ca^{2+}-bound structural states depicted the overall organization of the cTF and the transition between the inhibited and activated states. Nevertheless, due to insufficient resolution within the experimental density maps (>7 Å in the Tm and Tn regions), both papers lacked details of specific interactions among the cTF components.

Based on the cryo-EM model, Tn core domain (Fig. 1A, Tn core) consists of TnC (Fig. 1A, blue ribbons), and an IT-arm (Fig. 1A, IT arm) composed of the central part of TnI (Fig. 1A, red ribbons) and C-terminal part of TnT (e.g., TnT2) (Fig. 1A, cyan ribbons). The C-terminal part of TnI (Fig. 1A, red arrows) stabilizes the inhibited state of the cTF via interactions with actin and Tm. The detailed diagram of TnT is shown in Supplementary Information Appendix, Fig. S1A. The N-terminal part of TnT (e.g., TnT1) can be defined as having three main structural regions (5, 6): the N-terminal hypervariable region (human residues h1–75), which is not resolved in the cryo-EM maps; Tm binding site (residues h87–150 that form an α-helix visible in a cryo-EM map) (Fig. 1A, TnT1 cyan); and the disordered TnT1 linker (residues h151–200, not resolved in a cryo-EM map) that connects the TnT1 and TnT2 regions (Supplementary Information Appendix, Fig. S1A, linker). TnT1 is of particular importance for cTF functionality because it spans across the Tm overlap region and stabilizes the Tm head-to-tail interaction (5, 6, 21, 22). Biochemical experiments showed that TnT1 interaction with the junction region promotes Tm binding to F-actin (23, 24) and enhances cooperative binding of rigor myosin to Tm-decorated F-actin (24, 25). The importance of TnT1 extends into pathophysiology because it harbors several pathogenic variants, which cause cardiomyopathies in humans (Table 1).

Early structural (26) and biochemical (27, 28) studies predicted the coil-coiled overlap between TnT1 and Tm molecules that were later confirmed by crystallographic (29) and *in-silico* (30) studies. Nevertheless, a complete high-resolution picture of the molecular interactions of TnT1 in the context of the cTF is lacking due to insufficient resolution of the recently obtained cryo-EM structures of the reconstituted and native cTFs (5, 6). Here, we used frozen, hydrated native cardiac TFs to generate a 3.8-Å resolution cryo-EM map of the cTF junction region at relaxing Ca^{2+} levels (pCa = 8). We reveal novel interactions among Tm, TnT1, and actin that stabilize the off state of the cTF. Importantly, our data provide direct insights into mechanisms of pathogenic mutations in the TnT linked to cardiomyopathies in humans.

Table 1. Cardiomyopathy-linked pathogenic variants in *TNNT2* gene and their predicted by cryo-EM structural effects on the junction region.

Mutation	Disease	Primary citation	Ca^{2+} sensitivity	Proposed by cryo-EM effect of mutation
P77L	HCM	(53)	↑	Weakens TnT1 loop region interaction with actin
I79N	HCM	(68)	↑	Weakens TnT1 loop region interaction with actin
P80S	HCM	(69)	↑	Weakens TnT1 loop region interaction with actin
E83K	HCM	(70)	↑	May redirect TnT1 loop region from actin
D86A	HCM	(71)	↑	May redirect TnT1 loop region from actin
R92L	HCM	(72)	↑	May redirect TnT1 loop region from actin
R92Q	HCM	(68)	↑	May redirect TnT1 loop region from actin
R92W	HCM	(73, 74)	↑	May redirect TnT1 loop region from actin
R94C	HCM	(74)	↑	Weakens TnT1 helix region interaction with Tm
R94L	HCM	(75)	↑	Weakens TnT1 helix region interaction with Tm
R94H	HCM	(76)	↑	Weakens TnT1 helix region interaction with Tm
K97N	HCM	(77)	↑	Weakens TnT1 helix region interaction with actin
R113S	HCM	(*)	↑	Weakens TnT1 helix region interaction with Tm
K124N	HCM	(78)	↑	Weakens TnT1 helix region interaction with Tm
R130C	HCM	(73)	↑	Weakens TnT1 helix region interaction with Tm
R134G	DCM	(79)	↓	Enhances TnT1 helix region interaction with Tm
R144W	DCM	(80)	↓	Enhances TnT1 helix region interaction with Tm

* National Center for Biotechnology Information. ClinVar; [VCV001005011.2], https://www.ncbi.nlm.nih.gov/clinvar/variation/VCV001005011.2 bottom

Results

Previously, we determined the structure of the native cardiac TF at moderate resolution ranging between ∼8 and 11 Å (6). At that resolution, it was not possible to predict the interactions between cTF components at the molecular level. The resolution was low presumably due to the intrinsic mobility of the internal components of the cTF. To overcome this obstacle, we aimed for a different approach—a targeted reconstruction of individual parts of the complex. Owing to the crucial role of the junction region for the cTF regulation, we aimed to obtain its high resolution structure. It has been shown (5, 6) that TnT1 is better resolved in the structure of the cTF in the off state (low Ca^{2+}) due to the interaction of TnT1 with actin, which was absent in the structure of the activated cTF (high Ca^{2+}). We imaged cTF at low Ca^{2+} level (pCa 8). To achieve high resolution, we used 24,133 micrographs of frozen hydrated cTF to manually select the best filaments for a focused refinement of the junction region (Supplementary Information Appendix, Fig. S2). The overall resolution of the resultant density map (using FSC = 0.143 criterion) was 3.5 Å (Supplementary Information Appendix, Fig. S3A). The local resolution varied significantly from 9.7 Å resolution in the N-terminal lobe of TnC (Supplementary Information Appendix, Fig. S3B, blue arrow) to near atomic 3.8 Å resolution in the junction region (Supplementary Information Appendix, Fig. S3B) and 3.2 Å resolution in F-actin part (Supplementary Information Appendix, Fig. S3C) showing that core of the Tn complex (Supplementary Information Appendix, Fig. S3B, blue arrow) is the most flexible part of the cTF presented in the density map. For that reason, the junction region part of the density map was segmented out from the overall 3D reconstruction, filtered to 3.8 Å resolution (Fig. 1B) and used for modeling. The quality of the map is illustrated in Supplementary Information Appendix, Fig. S4.

Since the two strands of the cTF are not equivalent (5, 6) (Supplementary Information Appendix, Fig. S1B), we compared the junction region structures from the lower and upper strands. Alignment of the two structures revealed that positions of both actin and Tm were indistinguishable, while there was a small ∼2° clockwise azimuthal movement in the upper part of the TnT1 helix (residues 129 to 158) between the lower and upper junction structures (Supplementary Information Appendix, Movie S1). Therefore, all the intermolecular interactions between the Tm strands, and Tm cable with actin discussed below are equivalent for the two cTF strands. The TnT1 interactions with the Tm cable that differ between the two strands will be outlined in the corresponding section.

Structure and interstrand interactions of Tm

The interactions between the Tm strands in the TF were proposed based on X-ray crystallography of Tm fragments (31, 32). Our density map and corresponding atomic model are in agreement with those observed by X-ray crystallography. The C-terminal Tm coiled-coil is stabilized by a set of hydrophobic and polar interactions. The core component is comprised of apolar residues (Fig. 2B, blue atoms) that contribute to the stability of the coiled-coil by the hydrophobic interactions between residues at positions *a* and *d* (Fig. 2A, blue arrows) within the seven-residue heptad of Tm. This architecture is broken after residue A262 where the two helices begin to splay due to the larger side chains of Q263 and the bulky aromatic rings of Y267 located in the interior of the coiled-coil (Fig. 2B, red atoms). The splay of the C-terminal helix is important for formation of the junction (31, 32). In addition to the apolar core, canonical salt bridges between side chains K231/E236, R238/E243, and E259/K264 (Fig. 2B, magenta atoms) located in the *e* and *g* positions (Fig. 2A, magenta arrows) hold the strands together. The formation of interstrand salt bridges taper off near the end of the C-terminus to facilitate the C-terminal splaying. The last four amino acids within the Tm C-terminus do not follow the α-helical pattern and thus provide flexibility required to form the junction with the adjacent Tm's N-terminus. Similar to the C-terminus, the porcine α-Tm N-terminal strands are held by hydrophobic interactions between the two helices at positions *a* and *d* (Fig. 2A, blue arrows), which are marked in blue in Fig. 2C. Canonical salt bridges between the side chains of R21/E26, R35/E40, and K49/E54 (Fig. 2C, magenta atoms) in the *e* and *g* positions (Fig. 2A, magenta arrows) further stabilize the N-terminus of Tm. In addition, noncanonical ionic interactions at the *a* and *g* positions (Fig. 2A, cyan arrow), reported by Brown et al. (31), are observed between D14/K15 and D28/K29 (Fig. 2C, cyan atoms).

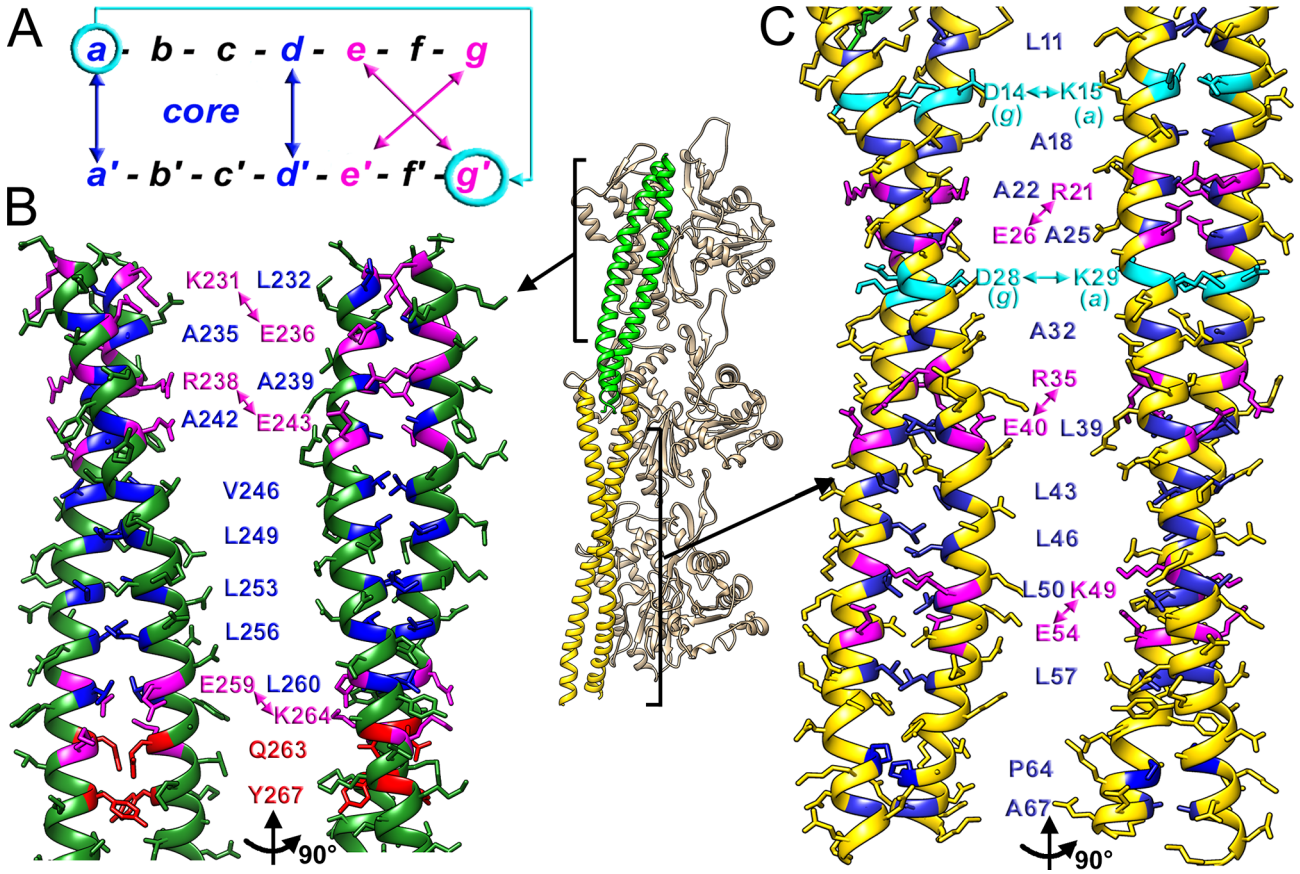

Fig. 2. The interstrand interactions of the α-Tm N' and C' termini of the cardiac native TF. (A) Diagram of the Tm seven-residue heptad. Residues in *a*/*a*' (blue double-headed arrow) and *d*/*d*' (blue double-headed arrow) heptad positions form hydrophobic core interactions (B and C, blue residues). Canonical salt bridges are formed by residues in *e*/*g*' (magenta double-headed arrow) and *e*'/*g* (magenta double-headed arrow), while noncanonical salt bridges have been observed between *a* and *g*' (cyan double-headed arrow). (B) Interactions between the Tm strands in the C-terminus (green ribbons) are comprised of hydrophobic interactions (blue atoms) and salt bridges (magenta atoms). The C-terminus begins to splay at Q263 (red atoms) and is separated further by the large side chains of Y267 (red atoms). (C) Interactions between the Tm stands in the N-terminus (gold ribbons) involve hydrophobic interactions (blue atoms) and salt bridges (magenta atoms). Two noncanonical salts bridges are shown in cyan.

Structure of the Tm junction region

The first structural data on the "head-to-tail" interactions between the two Tm molecules were obtained by NMR using Tm fragments in the absence of actin and TnT1 (17). Our atomic model overall confirms the main NMR findings regarding the structure of the Tm overlap region. A cluster of aliphatic amino acids is comprised of Tm N-terminal residues M1, A3, I4, M8, and L11 (Fig. 3, blue atoms) and Tm C-terminal residues L274, A277, L278, and M281 (Fig. 3, magenta residues) hold the N- and C- termini of the two adjacent Tm molecules together. K7 (Fig. 3, cyan atoms) contributes to the hydrophobic core via its aliphatic part. The ionic interaction between K5 and D280 (Fig. 3, red arrow) further stabilizes the Tm junction. Nevertheless, there is a difference between the cryo-EM and NMR-based models of the junction region in the C-terminal part of Tm. In our model, Tm's C-terminal residues (e.g., S283 and I284) do not bend toward the core of the junction, but rather face straight down toward the N-terminus of the adjacent Tm molecule (Supplementary Information Appendix, Fig. S5B, red arrow) so that I284 makes a hydrophobic interaction with the apolar part of K12 (Fig. 3, black arrow). This unbending of the Tm's C-terminus is observed on both Tm strands.

F-actin–Tm interactions

All the previous high resolution structures of Tm-bound actin complexes were obtained using helical averaging (33–36), which eliminated information on the Tm amino acids involved in the interaction with actin. The F-actin–Tm interface in our density map (Supplementary Information Appendix, Fig. S6) shows that only ionic interactions hold the visualized portion of Tm on the surface of F-actin (Fig. 4). Each α-Tm molecule spans the length of seven actin subunits and has seven-quasi-equivalent period repeats (13), each containing a pattern of amino acid residues previously predicted to be conserved actin-binding sites (14–16). Our model contains a fragment of period 6 (residues 230–242; Fig. 4, dark green ribbons) along with period 7 (residues 243–284; Fig. 4, green ribbons) of the Tm C-terminus, and period 1 (residues 1–46; Fig. 4, yellow ribbons) along with a fragment of period 2 (residues 47–70; Fig. 4, dark red ribbons) of the Tm N-terminus. This region of two adjacent Tm molecules spans the length of three actin subunits (Fig. 4, tan ribbons). First, all three actins in our model form salt bridges through their K326/K328 (Fig. 4, blue spheres) with the acidic residues of Tm periods 1 (D20/E23), 2 (D58/E62), and 7 (D254/E257) (Fig. 4, red spheres). Acetylation of these lysine residues in actin modulates striated muscle contraction (37). An-

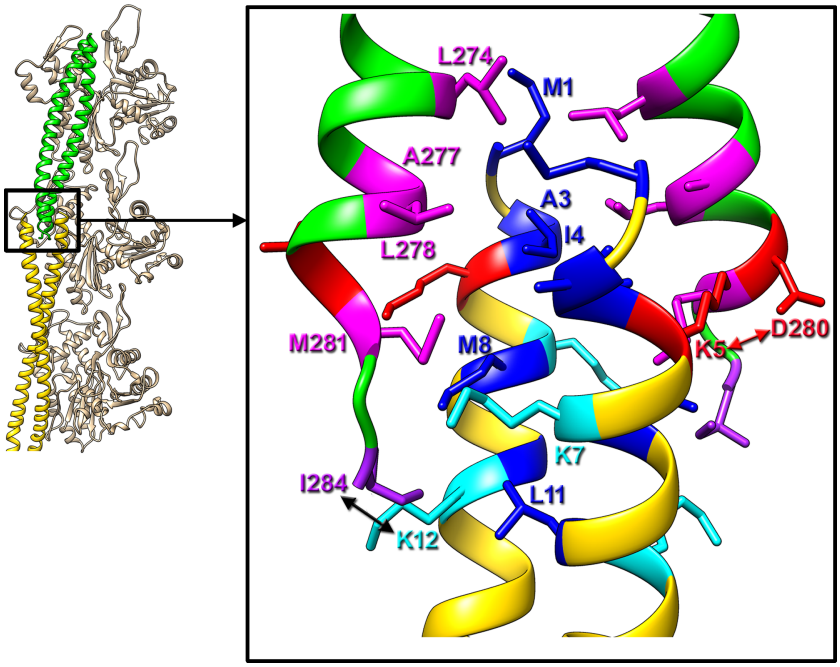

Fig. 3. The proposed intermolecular interactions of the α-Tm overlap region of the cardiac native TF. The Tm overlap region between the C-terminus (green ribbons) and the N-terminus (gold ribbons) of the adjacent Tm molecule spans three actin subunits (tan ribbons). The black box outlines the detailed part of the model. This part docked into the corresponding density map region is shown in Supplementary Information Appendix, Fig. S5A. The Tm C-terminal apolar residues are shown as magenta atoms, while hydrophobic residues located in the Tm N-terminus are shown as blue atoms. Charged residues that form ionic bonds are shown in red, while the two lysines (e.g., K7 and K12) that contribute to hydrophobic interactions are marked in cyan. Interaction between I284 and apolar part of K12 is marked with black arrow. The salt bridge between Tm D280 and K5 is marked with red arrow. Proposed interactions between C-terminus residues and N-terminus residues that stabilize the Tm overlap region are discussed in the text. The barbed end of actin is at the bottom.

other repetitive interaction found between Tm periods 6 and 7 is between K238 of actin and E240/D275 of Tm (Fig. 4, cyan and magenta spheres, respectively). The junction region interactions with actin are reinforced via two additional salt bridges between actin residues K215/E241 (Fig. 4, pink and purple spheres, respectively) and residues E272/K268 of the C-terminus of Tm (Fig. 4, dark blue and dark yellow spheres, respectively). Finally, period 7 makes one more ionic interaction via K248 (Fig. 4, gray spheres) with D311 of actin (Fig. 4, black spheres), which makes it the period that is most tightly attached to F-actin out of the four repeats present in our model. This tight attachment results from the geometry of the junction region where the internal strand of the Tm C-terminus lies in very close proximity to the surface of the actin filament.

Tm–TnT1 interactions with Tm and actin

CLUSTAL alignment of the human TNNT2 sequence (Uniprot P45379-6) with the porcine TNNT2 (Uniprot I3LS66) sequence reveals that the two homologs share 91% identity while possessing 95% identity in the TnT1 region presented in our atomic model (Supplementary Information Appendix, Fig. S7A). There is a shift in the numbering between the two isoforms, therefore, we will denote human numbering related to pathogenic mutations with "h" (e.g., hI79N). Actin isoforms are identical between the two species as well as Tm's N-terminus presented in the model, while Tm's C-terminus is 99% identical bearing one nonconserved substitution (Supplementary Information Appendix, Fig. S7B, purple arrow).

The TnT1 region of the cTF junction can be divided into two structural parts—a helical part (Fig. 1A, cyan and Supplementary Information Appendix, Fig. 1A, residues F96–R158) previously reported at low resolution (5, 6), and a loop portion (Supplementary Information Appendix, Fig. 1A, residues V84–D95) previously not defined in the cryo-EM maps. The TnT1 helical part stabilizes the Tm overlap region and "staples" it to the surface of the actin filament via both ionic and hydrophobic interactions (Fig. 5B to F). The upper part of the helix forms a set of salt bridges with the C-terminus of Tm (Fig. 5B and C, red atoms), which are different for the lower (Fig. 5B) and upper (Fig. 5C) strands due to the small azimuthal shift of this TnT1 region on Tm between the lower and the upper strand (Supplementary Information Appendix, Movie S1). In the lower strand, a TnT1 positively charged cluster composed of K131, R137, and R138 interacts with Tm D254, E257, and E259, respectively (Fig. 5B, red atoms). The upper strand (Fig. 5C) lacks the salt bridge between TnT1 R137 and Tm E257, although it forms an ionic bond between TnT1 R141 and Tm E250 (Supplementary Information Appendix, Fig. S9). The rest of the interactions between TnT1 and Tm/actin are identical between the two strands. Another charged TnT1 patch, located immediately above the junction region and composed of E124, E125, and R121, forms ionic bonds with Tm K266, K268, and E272, respectively (Fig. 5D). The central helical region of TnT1 (Fig. 5E, residues R103–F118) stabilizes the junction region via both hydrophobic (Fig. 5E, blue atoms) and ionic (Fig. 5E, red atoms) interactions. Specifically, TnT1 L110 and I114 (Fig. 5E, blue atoms) contribute to the hydrophobic cluster that holds together the Tm overlap region (Fig. 3). In addition, two salt bridges, one between H117 of TnT1 and D275 of Tm's C-terminus and the other between E109 of TnT1 and K6 of Tm's N-terminus (Fig. 5E, red atoms) reinforce the stability of the Tm junction. TnT1 R103 strengthens the interaction of TnT1 with Tm's N-terminus (Fig. 5E, red atoms). Since, the distances between the C-α atom of R103 and corresponding C-α atoms of Tm D14 and actin E334 are equivalent (11 and 10.5 Å, respectively), it is possible that

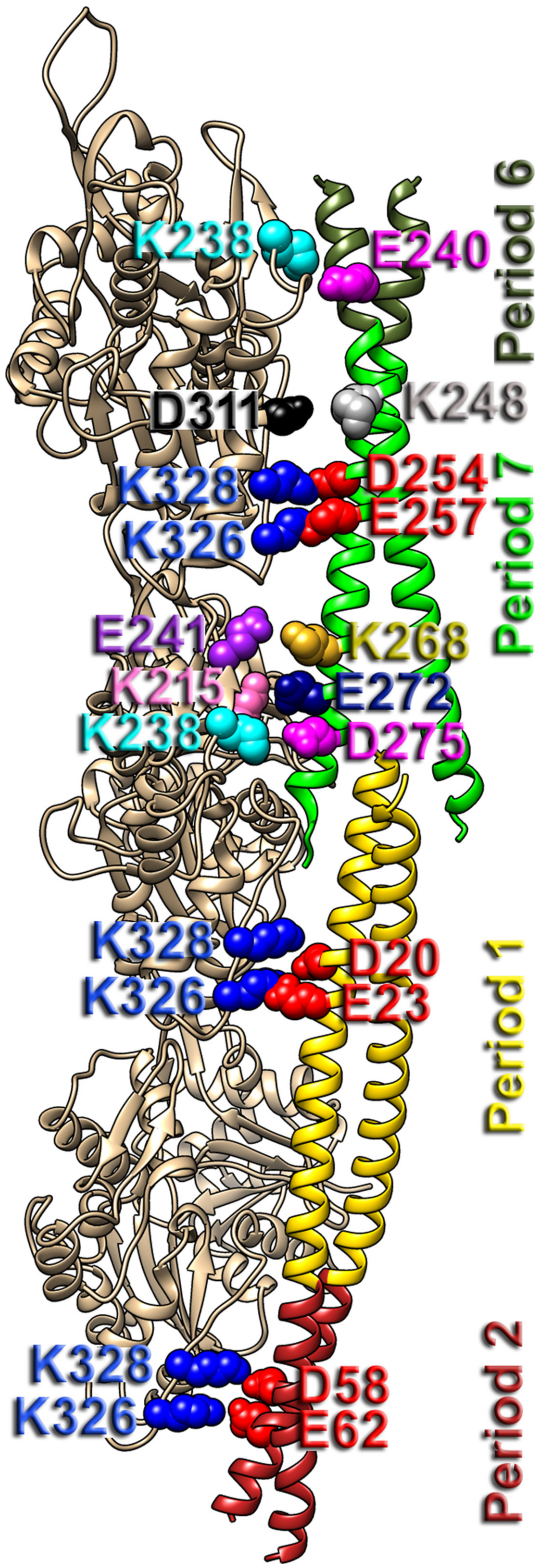

Fig. 4. Proposed interactions of the Tm coiled-coil with actin. Actin is shown in tan, while the Tm periods are shown in different colors. C-terminal periods 6 and 7 presented in the model are in dark and light green, respectively. N-terminal periods 1 and 2 are shown in gold and dark red, respectively. Actin and Tm residues involved in the ionic interactions (colored spheres) are discussed in the text. These residues with the corresponding regions of the density map are shown in Supplementary Information Appendix, Fig. S6. The barbed end of actin is at the bottom.

R103 may contribute to the ionic interactions between TnT1 and actin discussed below.

A positively charged TnT1 patch located below the Tm–Tm junction (Fig. 5F) stabilizes the junction region on the body of the actin filament via salt bridges, respectively, between K102 and K105 of TnT1 and D25 and E334 of actin (Fig. 5F, magenta atoms). Tethering of the junction region to F-actin stabilizes the off state of the cTF.

Twelve TnT1 residues (from D90 to R101) do not form any bonds with either Tm or actin despite the high content of charged residues. It is feasible that intrastrand ionic interactions (Fig. 5F, red arrows) involving E92, R93, D95, D98, and R101 (Fig. 5F, black atoms) provide the geometry and directionality of the loop that connects the two TnT1 actin-binding regions—one consisting of ionic interactions (Fig. 5F, magenta atoms) and the other formed by hydrophobic bonds (Fig. 5G, purple atoms) discussed below.

The lower portion of the TnT1 loop penetrates into the cavity between the D-loop of the lower actin subunit and C-terminus of the upper actin subunit to form a cluster of hydrophobic interactions, which is comprised of TnT1 P86, I88, and P89 and actin V45, M355, and F375 (Fig. 5G, purple atoms). These interactions further stabilize the off state of the cTF.

Discussion

Discovery of the role of Ca^{2+} levels in regulation of actomyosin interactions (1–3) initiated the search for molecular mechanisms underlying this vital process for striated muscle contraction. Early X-ray structural studies on living muscle, combined with preceding biochemical evidence, gave rise to a steric blocking model of muscle regulation that holds that at relaxing (low-Ca^{2+}) conditions, Tm blocks myosin-binding sites on the surface of F-actin, while at activating (high-Ca^{2+}) conditions, Tn complex moves Tm away from the myosin-binding sites (2). This was subsequently supported by solution kinetics data (18). Later, structural studies provided mechanistic support for this concept by directly showing the Ca^{2+}-induced azimuthal movement of the Tm cable on the surface of the TF (38). Further, structural studies using negatively stained (39) and frozen hydrated (40) TFs provided additional support for the steric blocking model, but due to the helical approach to 3D reconstruction, information on the structure of the Tn complex was omitted leaving the mechanism of TF regulation unresolved.

Innovative work by Yamada et al. (5) utilized a nonhelical algorithm to reconstruct the reconstituted cardiac TF and showed structural transition of the entire TF (e.g., including Tn complex) from Ca^{2+}-free to the Ca^{2+}-bound state. Their key findings were entirely confirmed using cardiac native TFs at physiological Ca^{2+} levels (6). These important studies enormously advanced our understanding of TF regulation, but due to intrinsic structural heterogeneity of the frozen hydrated cardiac TFs, they lacked sufficient resolution to reveal molecular details that underlie Ca^{2+}-regulatory function. For that reason, both papers omitted any discussions on the molecular interactions between the components of the cTF. Flexible fitting routines along with the molecular dynamics calculations were used to predict the missing information in cryo-EM maps on the interactions between actin, Tm, and TnT (41). We carefully compared the junction region of the resultant *in-silico* model of the cTF (PDB 7UTL) with the atomic model derived from the high resolution cryo-EM map (Supplementary Information Appendix, Fig. S10). We found that the structure of the actin filament was in general agreement, except the position of the D-loop of actin (Supplementary Information Appendix, Fig.

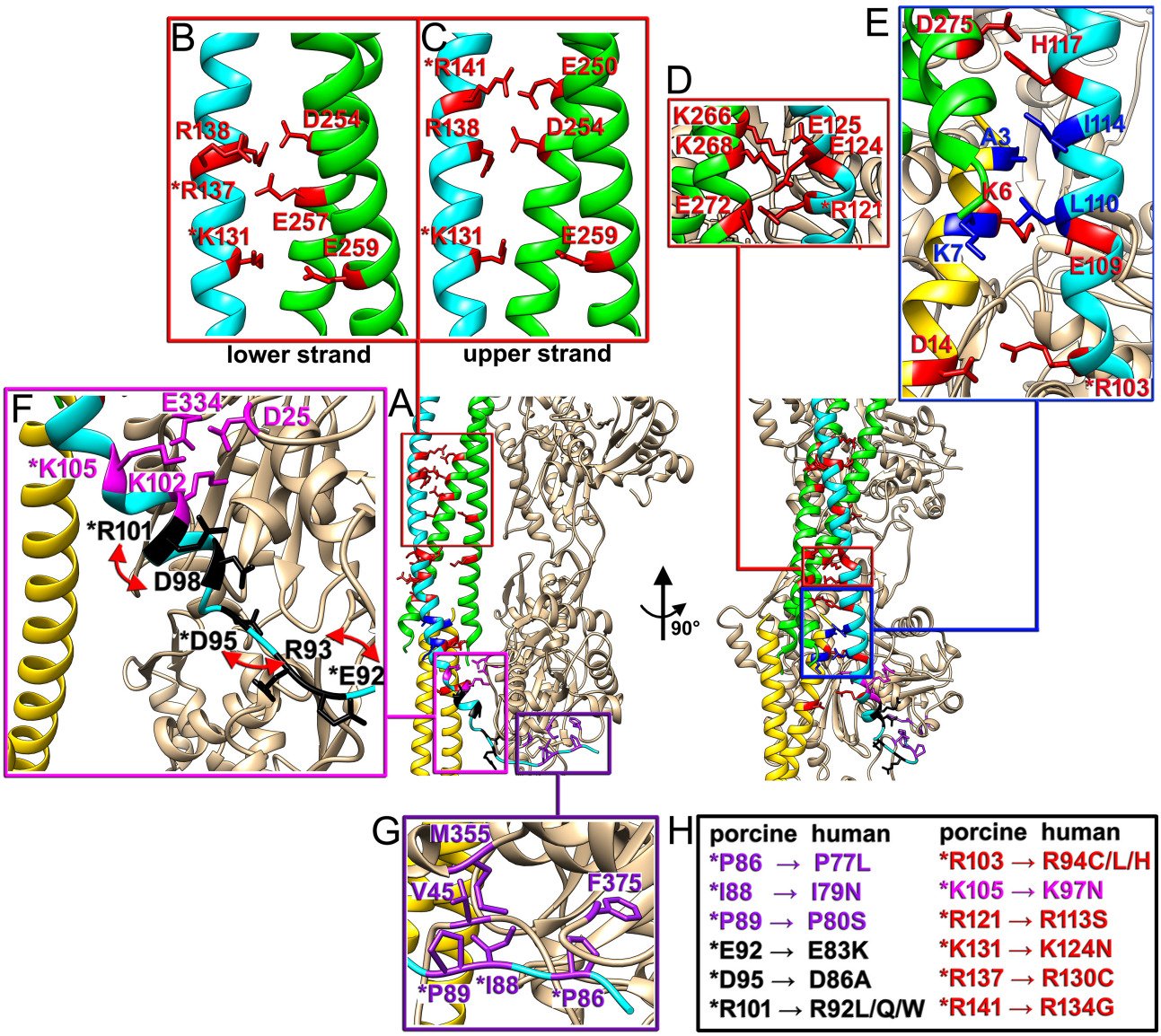

Fig. 5. Proposed interactions of TnT1 with Tm and actin. (A) Atomic model of the cTF junction region is shown having actin in tan, Tm's C-terminus in green, Tm's N-terminus in gold, and TnT1 in cyan ribbon. The two views of the same model are related by 90° azimuthal rotation. (B to G) Detailed views of TnT1 interface with Tm (B to E) and actin (F and G) are shown in colored boxes, which are related to the cTF junction region model shown in (A). TnT1 and Tm residues that form salt bridges are shown as red atoms, while TnT1 and Tm residues involved in hydrophobic interactions are shown as blue atoms. TnT1 and actin residues that form salt bridges are depicted as magenta atoms. TnT1 and actin residues that form a hydrophobic cluster under subdomain 1 of actin are outlined as purple atoms. TnT1 residues involved in preservation of the geometry of the TnT1 loop that connects the two actin-binding regions on TnT1 (i.e., ionic magenta and hydrophobic purple) are depicted as black atoms. Red arrows point to residue pairs that form salt bridges. Residues that have pathological variants linked to cardiomyopathies are marked with an asterisk. (H) TnT1 porcine and their corresponding pathogenic variants in humans are tabulated using the same color codes used in (B to G). Details of interactions are discussed in the text. The residues involved in TnT1 interactions with Tm and actin are shown along with the corresponding regions of the density map in Supplementary Information Appendix, Fig. S8.

S10A, red arrow). Key differences between the two models were found in the Tm overlap region, where the arrangement of the Tm N- and C-termini differed significantly (Supplementary Information Appendix, Fig. S10C, compare green/yellow with pink/purple ribbons), and in the position of the TnT1 helix on Tm surface (Supplementary Information Appendix, Fig. S10D, red arrow). Positioning of Tm cable on the surface of F-actin in the Pavadai et al. model was shifted by ~2.5 Å (Supplementary Information Appendix, Fig. S10A, compare green/yellow with pink/purple ribbons). Both models agree on the role of K326 and K328 of actin in making ionic interactions with the negatively charged residues of Tm (Supplementary Information Appendix, Fig. S10E, red atoms), while our model provides previously missing information on the ionic interactions of the Tm overlap region with actin (Supplementary Information Appendix, Fig. S10E, blue atoms). Overall, our model provides significant corrections to the previously available model of the junction region in the relaxed state. Determination of the junction region structure at activating Ca^{2+} levels is more challenging, but will be required for complete molecular characterization of this crucial cTF region.

Physiological implications of the junction structure for Ca^{2+}-regulation of cardiac muscle

The significance of this region for cTF regulation cannot be understated. Striated muscle regulation relies on allosteric structural coupling among its functional units (42, 43). To explain this coupling on the TF, considerable emphasis has been placed on the end-to-end ("head-to-tail") overlap interaction between adjacent Tm molecules where the Tm-binding segment of TnT1 is also found (44, 45). Our analysis of the relationships among adjacent cTF structural regulatory units suggests that there is cooperativity not only along Tm strands but also across the two Tm strands of the cTF, both of which are expected to involve portions of TnT1 (6); the analysis presented here will focus on the former because the latter involves presumably regions of TnT that have not yet been resolved (e.g., the linker region in Supplementary Information Appendix, Fig. S1A, residues h152–200). All our previous knowledge about the structure of the Tm molecule and the end-to-end overlap region came from X-ray crystallography (31, 32) and NMR (17) studies of isolated Tm fragments. Here, we show that the structures of the Tm N- and C-terminal regions within the native cTF (Fig. 2) are in agreement with the X-ray crystallography data (31, 32), which yields a rigorous model of the aforesaid Tm regions. We also provide the structure of the Tm overlap region (Fig. 3) that is crucial for the "head-to-tail" TF cooperativity. The structure of the junction region in its most native form (e.g., bound to actin and stabilized by the TnT1) is consistent with the solution structure of the isolated overlap complex (17), except the C-terminal Tm tail (e.g., residues S283 and I284), which in our structure bends down (Supplementary Information Appendix, Fig. S5B, red arrow). The reason for this discrepancy between cryo-EM and NMR data cannot be explained by the presence of actin or TnT1 in the cryo-EM structure because this type of straightening of the Tn C-terminus is observed on both strands irrespective of their interactions with either actin or TnT1. It is possible that stochastic interactions of the highly negatively charged TnT hypervariable N-terminus (Supplementary Information Appendix, Fig. S1A) with the junction region, not visible in the density map, lead to the Tm C-terminus rearrangements.

Extensive biochemical and structural data (5, 6, 21, 22) unambiguously show that the function of TnT1 is to stabilize the Tm junction by forming a five-helix coiled-coil that enhances the connection between adjacent TF regulatory units (24, 25). Our data obtained using native cTF fully confirm that TnT1 makes ionic and hydrophobic interactions (Fig. 5B to D, red and blue atoms, respectively) that link it to both C-terminal and N-terminal parts of Tm that form the overlap region. TnT1 also plays a role in the cooperativity between the two strands of Tm (6, 46), since its interaction with the junction region on the opposite strand of the TF provides a physical link between the two TF stands via TnT1 linker region (47).

The specific interactions identified in this study provide a structural basis to the inhibitory properties of TnT1 (48), and these interactions likely modulate important aspects of cardiac function beyond cooperative interactions between adjacent regulatory units. First, interactions of Tm and TnT1 with actin (e.g., Figs. 4 and 5) that stabilize the off state would influence how easily and how rapidly Ca^{2+} turns on the regulatory unit during systole and also the kinetics of returning to the off state and relaxation after Ca^{2+} dissociates during diastole. Second, interactions between the Tm monomers within a Tm molecule (e.g., Fig. 3) are expected to have a significant influence on the mechanical properties of individual Tm molecules. The flexibility of Tm is tuned for optimal Ca^{2+}-regulatory function (49, 50); therefore, Ca^{2+} sensitivity of the cTF may be affected by the Tm stiffness. Finally, the interaction of the loop region of TnT1 with actin that takes place only at relaxing conditions may modulate the rigidity of the cTFs, which depends on the Ca^{2+} level (51).

Pathophysiological implications of cardiomyopathy mutations on the junction structure for altered Ca^{2+} regulation of cardiac muscle

Not surprisingly, the TnT1 region is a major hotspot for cardiomyopathy causing mutations (52) with a high incidence of sudden cardiac death (53) and atrial fibrillation (54). Due to the absence of a high-resolution structure of the junction region of the cTF, the underlying molecular mechanisms of these mutations were unknown. Our model shows that a charged patch of TnT1 residues (i.e., R121, E124, E125, K131, R137, R138, and R141) located in the upper and middle part of TnT1 helix form a cluster of ionic bonds with the Tm C-terminus (Fig. 5B to D, red atoms), while a cluster of hydrophobic and ionic interactions (Fig. 5E, blue and red atoms, respectively) stabilize the overlap region. At the same time, the bottom of the TnT1 helix contains a cluster of positively charged residues that connect it to the surface of the actin filament (e.g., K102, and K105 in Fig. 5E). Therefore, as predicted earlier (5, 6) and confirmed here, TnT1 helix works as a joint that anchors the Tm junction region to actin and thus stabilizes the cTF inhibited state. We propose that mutations that weaken TnT1 helix interactions with either Tm or actin may lead to increased cTF Ca^{2+} sensitivity—a typical manifestation of Tn variants associated with HCM. In agreement with this prediction, HCM linked hK124N and hR130C mutations in TnT1 helix (Fig. 5H and Table 1) that should prevent formation of salt bridges between TnT1 and Tm's C-terminus (Fig. 5B and C), have been shown to reduce TnT1 affinity to Tm (55) and diminish its inhibitory properties by increasing Ca^{2+} sensitivity of the mutant cTF (56). Our data suggest that hR130C would impact only the lower strand Ca^{2+} sensitivity, since this interaction does not take place in the upper strand (Fig. 5B and C). Nevertheless, taking into account cooperativity between the two strands (6, 46), this mutation would impact the overall dynamics of the entire cTF. Another HCM-linked mutation that relates to our model predictions (e.g., hR113S, see Fig. 5H) has been recently reported (Table 1). HCM-linked hR94L mutation (porcine R103 in Fig. 5D) reduces the affinity of $TnT1_{70\text{-}170}$ fragment to Tm (27), which is consistent with R103 interaction with D14 of Tm N-terminus in our model (Fig. 5E). The hR94C mutation has been reported to increase muscle activation at resting and submaximal Ca^{2+} concentrations (57). HCM-linked hK97N mutation (Fig. 5H and Table 1), which is expected to disrupt TnT1 interaction with actin rather than with Tm (Fig. 5F), does not change the affinity of $TnT_{70\text{-}170}$ fragment to Tm while conferring increased Ca^{2+} sensitivity (54).

We show here that the loop region of TnT1 (e.g., V84–F96) makes a cluster of hydrophobic interactions with actin (Fig. 5G). These interactions along with ionic bonds between TnT1 and actin (Fig. 5F, magenta atoms) collectively stabilize the off state of the cTF. Therefore, mutations in TnT1 that would destabilize the interaction of the TnT1 loop with actin should confer increased myofilament Ca^{2+} sensitivity, which has been associated with the HCM phenotype. Consistent with this prediction, mutations in all the three TnT1 residues hP77L, hI79N, and hP80S (Fig. 5H and Table 1) are associated with HCM in humans.

The mouse model bearing the TnT hI79N mutation in the heart indeed displays increased Ca^{2+} sensitivity of contraction as well as clinical features of HCM (58). Both hI79N (27, 59) and hP80S (55) do not affect TnT1 affinity to Tm, because these residues contribute to actin binding and are distal from the Tm junction region, while they increase Ca^{2+} sensitivity of the cTF carrying either of the two pathogenic variants (55, 60, 61). We could not find any biochemical or physiological measurements for the hP77L but it is likely that its pathogenic mechanism is similar to hI79N and hP80S.

The geometry of the TnT1 region that links the two TnT1 actin-binding sites (residues E92–R101) is maintained by intrastrand ionic interactions involving E92, R93, D95, D98 and R101 (Fig. 5F, black atoms). Our model predicts that alteration of these salt bridges by charge-eliminating or charge-flipping mutations may redirect the TnT1 hydrophobic residues (e.g., P86, I88, and P89) away from their actin counterparts (e.g., V45, M355, and F375) and prevent formation of the hydrophobic cluster (Fig. 5G, purple atoms). In such an event, the off state of the cTF will be destabilized, leading to increased cTF Ca^{2+}-binding affinity, and consequently HCM. Consistent with this, hE83K, hD86A, hR92Q, and hR92L mutations were linked to HCM in humans (Table 1 and Fig. 5H). hR92Q and hR92L pathogenic variants markedly increase myofilament Ca^{2+} sensitivity (54, 62). An alternative explanation would be that these HCM-linked mutations may affect the interaction of the TnT1 with Tm in the activated cTF when TnT1 dissociates from the actin surface (5, 6).

The DCM-linked hR134G and hR144W mutations (Table 1) have been shown to increase TnT1 affinity to Tm and reduce TF Ca^{2+} sensitivity (55). In the absence of mutation, TnT1 R141 (hR134) is positioned against another positively charged residue, K248 of Tm (Supplementary Information Appendix, Fig. S11A and B, orange arrows). The R134G mutation may increase affinity of TnT1 to Tm by attenuating the repulsive force between those two residues. This would be especially effective in the lower strand where R141 does not make a salt bridge with E250 (Supplementary Information Appendix, Fig. S11A), in contrast to the upper strand (Supplementary Information Appendix, Fig. S11B, red arrow). Arginine substitution to a small, uncharged glycine in hR134G should eliminate the repulsive forces and lead to tighter TnT1 binding to Tm, enhanced stabilization of the inhibited cTF state, and reduced myofilament Ca^{2+} sensitivity (i.e., more Ca^{2+} is required to turn on the cTF), which is a hallmark of DCM. hR144W (porcine R151) mutation may lead to a novel bond between the aromatic rings of the tryptophan introduced into TnT1 and phenylalanine in Tm (Supplementary Information Appendix, Fig. S11C), which may enhance TnT1 binding to Tm to promote DCM phenotype due to overstabilization of the off state of the cTF. Further structural work is required to understand the molecular mechanisms of DCM in cTFs carrying these two pathogenic TnT1 variants.

To conclude, our model of the cTF junction region provides valuable structural information regarding the possible pathogenic mechanisms of the cardiomyopathy-linked mutations based on the immediate effect of the mutation on the observed inter- and intramolecular interactions. Nevertheless, taking into account possible allosteric coupling between the cTF elements, subsequent structural studies on each and every pathogenic variant will be required to establish how these mutations affect the overall structural state of the cTF.

Our data also confirms previous observations (5, 6) that the two strands of the cTF are not equivalent. The shift in positioning of the upper part of the TnT1 helix between the two strands (Supplementary Information Appendix, Movie S1) and resultant differences in the TnT1 interaction with Tm on the two strands (Fig. 5B and C, Supplementary Information Appendix, Fig. 9A and B) may be caused by alterations in the positioning of the linker region (Supplementary Information Appendix, Fig. S1A, residues h152–200) on the two strands of the cTF. Therefore, the differences in the TnT1 interaction with Tm on each of the two strands that we observe may underlie the molecular mechanisms that give rise to the variance in the cooperativity between the two strands of the cTF upon Ca^{2+} activation (6). The effect of the pathogenic mutations on the structural state of the cTF may also differentiate between the two strands and this requires experimental elucidation.

In summary, our work provides a detailed high-resolution structure of the junction region of native cTF. Specific molecular interactions identified here could be the subject of future mutagenesis studies to quantitatively evaluate their contributions to structure and function. Naturally occurring isoform differences in coupling between adjacent regulatory units result in the functional regulatory unit size of skeletal muscle TFs (63) being longer than that for cardiac muscle (64). Thus, it will be of great interest to determine the structure of the junction region of skeletal muscle TFs for comparison with the current structure in cTFs. Furthermore, careful design of experiments that involve myosin S1 will be important for discerning the roles of structural elements (particularly TnT1) for cross-bridge formation and force generation.

Materials and Methods

Proteins and buffers

Native porcine cardiac TFs were prepared as described in ref. (6). A-buffer was used for cryo-EM experiments: 50 mM potassium acetate, 10 mM 3-(N-morpholino) propane sulfonic acid (MOPS), 3 mM $MgCl_2$, and 2.0 mM (ethyleneglycol-bis(β-aminoethyl ether)-N,N,N′,N′-tetraacetic acid (EGTA) (pCa 8). The pH was adjusted to 7.0 after all of the components were mixed.

Cryo EM

A total of 1.8 μL of 1 μM native TFs in A-buffer Ca^{2+}-free (pCa 8) conditions was applied to the center of the glow discharged lacey carbon grid so that they form a small droplet in the center of the grid. The small droplet was immediately blotted with Whatman Grade 1 filter paper for 3 to 5 s and vitrified in a Vitrobot Mark IV (FEI, Inc.). Summary for imaging conditions and image reconstruction is provided in Supplementary Information Appendix Table S1. Image analysis was performed using RELION (65), while modeling was done using UCSF Chimera (66) and PHENIX software suites (67). Model validation statistics is provided in Supplementary Information Appendix Table S2. Experimental details are provided in the Supplementary Information "Materials and Methods."

Acknowledgments

We thank Dr Gunnar F. Schröder (Institute of Biological Information Processing, Forschungszentrum Jülich, Germany) for his comments and suggestions regarding the map and the model.

Supplementary Material

Supplementary material is available at *PNAS Nexus* online.

Funding

This work was supported by NIH grants R01 HL160966 (to V.E.G., J.R.P, and P.B.C), R01 HL140925 (to V.E.G. and H.D.W.), U24 GM116790 (to V.E.G.), and S10-RR025067.

Data Availability

The atomic model has been deposited at the Protein Data Bank (www.rcsb.org) with accession code 8DD0, while its corresponding cryo-EM map was deposited in the Electron Microscopy Data Bank (www.ebi.ac.uk/pdbe/emdb) with accession code EMD- 27,331.

References

1. Ebashi S, Endo M. 1968. Calcium ion and muscle contraction. Prog Biophys Mol Biol. 18:123–183.
2. Huxley HE. 1972. Structural changes in the actin- and myosin-containing filaments during contraction. Cold Spring Harbor Symp Quant Biol. 37:361–376.
3. Spudich JA, Huxley HE, Finch JT. 1972. Regulation of skeletal muscle contraction. II. Structural studies of the interaction of the tropomyosin-troponin complex with actin. J Mol Biol. 72:619–632.
4. Vibert P, Craig R, Lehman W. 1997. Steric-model for activation of muscle thin filaments. J Mol Biol. 266:8–14.
5. Yamada Y, Namba K, Fujii T. 2020. Cardiac muscle thin filament structures reveal calcium regulatory mechanism. Nat Commun. 11:153.
6. Risi CM, *et al.* 2021. The structure of the native cardiac thin filament at systolic Ca^{2+} levels. Proc Natl Acad Sci USA. 118:e2024288118.
7. Szent-Gyorgyi AG, Cohen C. 1957. Role of proline in polypeptide chain configuration of proteins. Science. 126:697–698.
8. Cohen C, Holmes KC. 1963. X-ray diffraction evidence for α-helical coiled-coils in native muscle. J Mol Biol. 6:423–IN11.
9. Corsi A, Perry SV. 1958. Some observations on the localization of myosin, actin and tropomyosin in the rabbit myofibril. Biochem J. 68:12–17.
10. Laki K, Maruyama K, Kominz DR. 1962. Evidence for the interaction between tropomyosin and actin. Arch Biochem Biophys. 98:323–330.
11. Flicker PF, Phillips GN, Cohen C. 1982. Troponin and its interactions with tropomyosin. An electron microscope study. J Mol Biol. 162:495–501.
12. Cohen C, Parry DA. 1990. α-Helical coiled coils and bundles: how to design an α-helical protein. Proteins. 7:1–15.
13. Phillips GN, Jr. 1986. Construction of an atomic model for tropomyosin and implications for interactions with actin. J Mol Biol. 192:128–131.
14. Barua B, Pamula MC, Hitchcock-DeGregori SE. 2011. Evolutionarily conserved surface residues constitute actin binding sites of tropomyosin. Proc Natl Acad Sci USA. 108:10150–10155.
15. Barua B, Winkelmann DA, White HD, Hitchcock-DeGregori SE. 2012. Regulation of actin–myosin interaction by conserved periodic sites of tropomyosin. Proc Natl Acad Sci USA. 109:18425–18430.
16. Barua B, Fagnant PM, Winkelmann DA, Trybus KM, Hitchcock-DeGregori SE. 2013. A periodic pattern of evolutionarily conserved basic and acidic residues constitutes the binding interface of actin-tropomyosin. J Biol Chem. 288:9602–9609.
17. Greenfield NJ, *et al.* 2006. Solution NMR structure of the junction between tropomyosin molecules: implications for actin binding and regulation. J Mol Biol. 364:80–96.
18. McKillop DFA, Geeves MA. 1993. Regulation of the interaction between actin and myosin subfragment-1: evidence for three states of the thin filament. Biophys J. 65:693–701.
19. Parmacek MS, Solaro RJ. 2004. Biology of the troponin complex in cardiac myocytes. Prog Cardiovasc Dis. 47:159–176.
20. Gordon AM, Homsher E, Regnier M. 2000. Regulation of contraction in striated muscle. Physiol Rev. 80:853–924.
21. Jackson P, Amphlett GW, Perry SV. 1975. The primary structure of troponin T and the interaction with tropomyosin. Biochem J. 151:85–97.
22. Pearlstone JR, Smillie LB. 1977. The binding site of skeletal alpha-tropomyosin on troponin-T. Can J Biochem. 55:1032–1038.
23. Hill LE, Mehegan JP, Butters CA, Tobacman LS. 1992. Analysis of troponin-tropomyosin binding to actin. Troponin does not promote interactions between tropomyosin molecules. J Biol Chem. 267:16106–16113.
24. Hinkle A, Goranson A, Butters CA, Tobacman LS. 1999. Roles for the troponin tail domain in thin filament assembly and regulation. A deletional study of cardiac troponin T. J Biol Chem. 274:7157–7164.
25. Schaertl S, Lehrer SS, Geeves MA. 1995. Separation and characterization of the two functional regions of troponin involved in muscle thin filament regulation. Biochemistry. 34:15890–15894.
26. Cabral-Lilly D, Tobacman LS, Mehegan JP, Cohen C. 1997. Molecular polarity in tropomyosin-troponin T co-crystals. Biophys J. 73:1763–1770.
27. Palm T, Graboski S, Hitchcock-DeGregori SE, Greenfield NJ. 2001. Disease-causing mutations in cardiac troponin T: identification of a critical tropomyosin-binding region. Biophys J. 81:2827–2837.
28. Palm T, Greenfield NJ, Hitchcock-DeGregori SE. 2003. Tropomyosin ends determine the stability and functionality of overlap and troponin T complexes. Biophys J. 84:3181–3189.
29. Murakami K, *et al.* 2008. Structural basis for tropomyosin overlap in thin (actin) filaments and the generation of a molecular swivel by troponin-T. Proc Natl Acad Sci USA. 105:7200–7205.
30. Pavadai E, Rynkiewicz MJ, Ghosh A, Lehman W. 2020. Docking troponin T onto the tropomyosin overlapping domain of thin filaments. Biophys J. 118:325–336.
31. Brown JH, *et al.* 2001. Deciphering the design of the tropomyosin molecule. Proc Natl Acad Sci USA. 98:8496–8501.
32. Li Y, *et al.* 2002. The crystal structure of the C-terminal fragment of striated-muscle α-tropomyosin reveals a key troponin T recognition site. Proc Natl Acad Sci USA. 99:7378–7383.
33. Behrmann E, *et al.* 2012. Structure of the rigor actin-tropomyosin-myosin complex. Cell. 150:327–338.
34. von der Ecken J, *et al.* 2015. Structure of the F-actin–tropomyosin complex. Nature. 519:114–117.
35. Risi C, *et al.* 2021. High-resolution cryo-EM structure of the cardiac actomyosin complex. Structure. 29:50–60.
36. Doran MH, *et al.* 2020. Cryo-EM and molecular docking shows myosin loop 4 contacts actin and tropomyosin on thin filaments. Biophys J. 119:821–830.
37. Schmidt W, Madan A, Foster DB, Cammarato A. 2020. Lysine acetylation of F-actin decreases tropomyosin-based inhibition of actomyosin activity. J Biol Chem. 295:15527–15539.
38. Lehman W, Craig R, Vibert P. 1994. Ca^{2+}-induced tropomyosin movement in *Limulus* thin filaments revealed by three-dimensional reconstruction. Nature. 368:65–67.

39. Pirani A, *et al.* 2005. Single particle analysis of relaxed and activated muscle thin filaments. J Mol Biol. 346:761–772.
40. Risi C, *et al.* 2017. Ca^{2+}-induced movement of tropomyosin on native cardiac thin filaments revealed by cryoelectron microscopy. Proc Natl Acad Sci USA. 114:6782–6787.
41. Pavadai E, Lehman W, Rynkiewicz MJ. 2020. Protein–protein docking reveals dynamic interactions of tropomyosin on actin filaments. Biophys J. 119:75–86.
42. Lehrer SS, Geeves MA. 1998. The muscle thin filament as a classical cooperative/allosteric regulatory system. J Mol Biol. 277:1081–1089.
43. Maytum R, Lehrer SS, Geeves MA. 1999. Cooperativity and switching within the three-state model of muscle regulation. Biochemistry. 38:1102–1110.
44. Pan BS, Gordon AM, Luo ZX. 1989. Removal of tropomyosin overlap modifies cooperative binding of myosin S-1 to reconstituted thin filaments of rabbit striated muscle. J Biol Chem. 264:8495–8498.
45. Lehrer SS, Golitsina NL, Geeves MA. 1997. Actin-tropomyosin activation of myosin subfragment 1 atpase and thin filament cooperativity. The role of tropomyosin flexibility and end-to-end interactions. Biochemistry. 36:13449–13454.
46. Manning EP, Tardiff JC, Schwartz SD. 2011. A model of calcium activation of the cardiac thin filament. Biochemistry. 50:7405–7413.
47. Deranek AE, Baldo AP, Lynn ML, Schwartz SD, Tardiff JC. 2022. Structure and dynamics of the flexible cardiac troponin T linker domain in a fully reconstituted thin filament. Biochemistry. 61:1229–1242.
48. Tobacman LS, *et al.* 2002. The troponin tail domain promotes a conformational state of the thin filament that suppresses myosin activity. J Biol Chem. 277:27636–27642.
49. Loong CK, Zhou HX, Chase PB. 2012. Persistence length of human cardiac α-tropomyosin measured by single molecule direct probe microscopy. PLoS One. 7:e39676.
50. Loong CK, Badr MA, Chase PB. 2012. Tropomyosin flexural rigidity and single Ca^{2+} regulatory unit dynamics: implications for cooperative regulation of cardiac muscle contraction and cardiomyocyte hypertrophy. Front Physiol. 3:80.
51. Isambert H, *et al.* 1995. Flexibility of actin filaments derived from thermal fluctuations. Effect of bound nucleotide, phalloidin, and muscle regulatory proteins. J Biol Chem. 270:11437–11444.
52. Tobacman LS, Cammarato A. 2021. Cardiomyopathic troponin mutations predominantly occur at its interface with actin and tropomyosin. J Gen Physiol. 153(3):e202012815.
53. Varnava AM, *et al.* 2001. Hypertrophic cardiomyopathy: histopathological features of sudden death in cardiac troponin T disease. Circulation. 104:1380–1384.
54. Pioner JM, *et al.* 2022. Genotype-driven pathogenesis of atrial fibrillation in hypertrophic cardiomyopathy: the case of different *TNNT2* mutations. Front Physiol. 13:864547.
55. Gangadharan B, *et al.* 2017. Molecular mechanisms and structural features of cardiomyopathy-causing troponin T mutants in the tropomyosin overlap region. Proc Natl Acad Sci USA. 114:11115–11120.
56. Madan A, *et al.* 2020. *TNNT2* mutations in the tropomyosin binding region of TNT1 disrupt its role in contractile inhibition and stimulate cardiac dysfunction. Proc Natl Acad Sci USA. 117:18822–18831.
57. Ezekian JE, *et al.* 2020. Variant R94C in *TNNT2*-encoded troponin T predisposes to pediatric restrictive cardiomyopathy and sudden death through impaired thin filament relaxation resulting in myocardial diastolic dysfunction. J Am Heart Assoc. 9:e015111.
58. Baudenbacher F, *et al.* 2008. Myofilament Ca^{2+} sensitization causes susceptibility to cardiac arrhythmia in mice. J Clin Invest. 118:3893–3903.
59. Lin D, Bobkova A, Homsher E, Tobacman LS. 1996. Altered cardiac troponin T in vitro function in the presence of a mutation implicated in familial hypertrophic cardiomyopathy. J Clin Invest. 97:2842–2848.
60. Yanaga F, Morimoto S, Ohtsuki I. 1999. Ca^{2+} sensitization and potentiation of the maximum level of myofibrillar ATPase activity caused by mutations of troponin T found in familial hypertrophic cardiomyopathy. J Biol Chem. 274:8806–8812.
61. Szczesna D, *et al.* 2000. Altered regulation of cardiac muscle contraction by troponin T mutations that cause familial hypertrophic cardiomyopathy. J Biol Chem. 275:624–630.
62. Messer AE, *et al.* 2016. Mutations in troponin T associated with Hypertrophic Cardiomyopathy increase Ca^{2+}-sensitivity and suppress the modulation of Ca^{2+}-sensitivity by troponin I phosphorylation. Arch Biochem Biophys. 601:113–120.
63. Regnier M, *et al.* 2002. Thin filament near-neighbour regulatory unit interactions affect rabbit skeletal muscle steady-state force-Ca^{2+} relations. J Physiol. 540:485–497.
64. Gillis TE, Martyn DA, Rivera AJ, Regnier M. 2007. Investigation of thin filament near-neighbour regulatory unit interactions during force development in skinned cardiac and skeletal muscle. J Physiol. 580:561–576.
65. Scheres SH. 2012. RELION: implementation of a Bayesian approach to cryo-EM structure determination. J Struct Biol. 180:519–530.
66. Pettersen EF, *et al.* 2004. UCSF Chimera—a visualization system for exploratory research and analysis. J Comput Chem. 25:1605–1612.
67. Liebschner D, *et al.* 2019. Macromolecular structure determination using X-rays, neutrons and electrons: recent developments in Phenix. Acta Crystallogr D Struct Biol. 75:861–877.
68. Thierfelder L, *et al.* 1994. α-Tropomyosin and cardiac troponin T mutations cause familial hypertrophic cardiomyopathy: a disease of the sarcomere. Cell. 77:701–712.
69. Otsuka H, *et al.* 2012. Prevalence and distribution of sarcomeric gene mutations in Japanese patients with familial hypertrophic cardiomyopathy. Circ J. 76:453–461.
70. Mogensen J, *et al.* 2003. Comparison of fluorescent SSCP and denaturing HPLC analysis with direct sequencing for mutation screening in hypertrophic cardiomyopathy. J Med Genet. 40:59e.
71. Van Driest SL, *et al.* 2003. Prevalence and spectrum of thin filament mutations in an outpatient referral population with hypertrophic cardiomyopathy. Circulation. 108:445–451.
72. Forissier JF, *et al.* 1996. Codon 102 of the cardiac troponin T gene is a putative hot spot for mutations in familial hypertrophic cardiomyopathy. Circulation. 94:3069–3073.
73. Koga Y, *et al.* 1996. Clinical manifestations of hypertrophic cardiomyopathy with mutations in the cardiac beta-myosin heavy chain gene or cardiac troponin T gene. J Card Fail. 2:S97–S103.
74. D'Cruz LG, *et al.* 2000. Cytosine methylation confers instability on the cardiac troponin T gene in hypertrophic cardiomyopathy. J Med Genet. 37:E18.
75. Varnava A, *et al.* 1999. A new mutation of the cardiac troponin T gene causing familial hypertrophic cardiomyopathy without left ventricular hypertrophy. Heart. 82:621–624.
76. Millat G, *et al.* 2010. Prevalence and spectrum of mutations in a cohort of 192 unrelated patients with hypertrophic cardiomyopathy. Eur J Med Genet. 53:261–267.

77. Coppini R, *et al.* 2014. Clinical phenotype and outcome of hypertrophic cardiomyopathy associated with thin-filament gene mutations. J Am Coll Cardiol. 64:2589–2600.
78. An FS, *et al.* 2004. [A novel missense mutation, K124N, in the troponin T gene of Chinese populations with hypertrophic cardiomyopathy]. Zhonghua Yi Xue Za Zhi. 84: 1340–1343.
79. Hershberger RE, *et al.* 2009. Clinical and functional characterization of TNNT2 mutations identified in patients with dilated cardiomyopathy. Circ Cardiovasc Genet. 2:306–313.
80. Rani DS, Dhandapany PS, Nallari P, Narasimhan C, Thangaraj K. 2014. A novel arginine to tryptophan (R144W) mutation in troponin T (*cTnT*) gene in an Indian multigenerational family with dilated cardiomyopathy (FDCM). PLoS One. 9:e101451.